Supporting Information

Paravastu *et al*. 10.1073/pnas.0806270105

SI Text

Fibril Preparation. $A\beta_{1-40}$ (sequence DAEFRHDSGYEVHHQKLVFFAEDVGSNKGAIIGLMVGGVV) was synthesized by fluorenylmethoxycarbonyl (FMOC) chemistry with *H*-benzotriazol-1-yl-tetramethyluronium hexafluorophosphate (HBTU) activation, using an Applied Biosystems Model 433A automated peptide synthesizer and procedures similar to those described previously (1–4). Uniformly ^{15}N,^{13}C-labeled residues were placed at positions summarized in Table 1. Placement of isotopic labels was chosen to avoid overlapping signals in 2D NMR spectra, and to probe hypothesized inter-sidechain proximities. Peptides were purified by reverse-phase HPLC at 55°C, using a Vydac C18 column and a water/acetonitrile gradient with 0.1% trifluoroacetic acid, and subsequently lyophilized. Purity was determined to be >95% using electrospray ionization mass spectrometry.

The initial $A\beta_{1-40}$ fibril sample was prepared by dissolving 1 mg of lyophilized, purified peptide in 10 mM Na_2HPO_4 to achieve a peptide concentration of 210 μM in a 1.5 ml tube. All aqueous solutions in this study also contained 0.01% NaN_3. The tube was inverted every minute for ≈10 min, until the disappearance of visible undissolved peptide. The solution was then dialyzed (1 kDa cutoff) for 1 h against a 1.5 l bath of pH 7.4 buffer (10 mM phosphate), then transferred to a new 1.5 ml tube and placed inside a bath sonicator (Branson model 2150). The sonicator was equipped with a timer set to sonicate for 30 s every hour. Fibrils were allowed to form with occasional sonication for 9 days, with monitoring of fibril formation by TEM. We refer to this sample as fibril generation 1.

Generation 2 fibrils were formed by addition of seeds from generation 1 to a fresh $A\beta_{1-40}$ solution, initially prepared in the same way as described for generation 1. In general, a seed solution was an aliquot of the previous fibril generation, fragmented by 10 min of bath sonication (Cole-Parmer ultrasonic cleaner) immediately before addition to freshly dissolved $A\beta_{1-40}$ (Fig. S1). The mass of $A\beta_{1-40}$ fibrils used to seed generation 2 was ≈5% of the mass of freshly dissolved $A\beta$. The seeded generation 2 solution was placed in the bath sonicator and subjected to occasional sonication (30 s per hr) for 7 days.

Subsequent generations were prepared using a modified protocol designed to minimize uncontrolled fibril nucleation. Lyophilized $A\beta_{1-40}$ was initially dissolved at 5.8 mM concentration in dimethyl sulfoxide (DMSO), allowed to sit for 5 min, and then diluted to 210 μM in 10 mM Na_2HPO_4. DMSO was removed by dialysis for 1 h against a 1.5 l bath of 10 mM phosphate buffer at pH 7.4. Dialyzed solutions were then filtered using 0.22 μm filters, placed in polypropylene tunes (BD Biosciences), and mixed immediately with seed solutions. Fibril generation $n + 1$ was the result of seeding with fibril generation n, and only 1 h for fibril growth was allowed between generations up to generation 12. This procedure successfully isolated a single fibril morphology, as shown in Fig. S1. The mass of $A\beta_{1-40}$ used to create each fibril generation was gradually increased until generation 12 contained 10 mg of $A\beta_{1-40}$.

To optimize fibril yields for solid state NMR experiments, peptide solutions corresponding to generations 12–15 were seeded by adding 10% seeds (by mass of $A\beta_{1-40}$). Seeded solutions were further "self-seeded" 2–24 h after initial seeding. Self-seeding was performed by one of two methods: (*i*) by brief sonication of the entire solution for 60 s in a bath sonicator, or (*ii*) by removal of an aliquot (5% by volume), bath sonication of this aliquot for 5 min, and addition of the sonicated aliquot back to the original solution. Fibrils were collected for NMR experiments one week after initial seeding, as described below, or solutions were frozen rapidly in liquid nitrogen and stored in a −20°C freezer for later use as seeds.

Electron Microscopy. TEM images were recorded at 26,000x magnification with a Philips/FEI CM120 transmission electron microscope. To prepare TEM samples, small aliquots (≈5 μl) of fibril solutions were diluted 10-fold with deionized water before being deposited onto freshly glow-discharged carbon films, supported by lacy carbon films on 200 mesh copper grids. Drops of diluted fibril solution, 5 μl in volume, were adsorbed to the carbon films for 2 min, and then excess fluid was blotted away. Grids were rinsed by applying 5 μl drops of deionized water for 1 min, followed by blotting. Finally, samples were negatively stained by applying 5 μl of 3% uranyl acetate for 1 min, followed by blotting and drying in air.

Samples for STEM were prepared by applying 5 μl drops of a series of solutions in rapid succession (without allowing surfaces to dry) to freshly glow-discharged carbon films, ≈3 nm in thickness, on copper grids. The first drop was an $A\beta_{1-40}$ fibril solution, diluted 10- to 20-fold in deionized water. After allowing 2 min for adsorption, the fibril solution was blotted away using filter paper. A drop of deionized water was then applied and blotted away after 1 min. Tobacco mosaic virus (TMV) solution was then applied and allowed to adsorb for 1 min. Finally, five 5 μl drops of deionized water were applied and blotted away in rapid succession. STEM images were recorded in a VG Microscopes HB501 field-emission STEM at an accelerating voltage of 100 kV, using a 1 nm probe diameter and an electron dose of ≈10^3 e/nm^2. STEM images were analyzed with ImageJ software (available at http://rsb.info.nih.gov/ij/) to generate a mass-per-length (MPL) histogram as described previously (2, 4). To minimize aggregation of fibrils that would complicate image analysis, STEM measurements were made less than 30 h after fibril seeding.

Atomic Force Microscopy. AFM images of fully hydrated $A\beta_{1-40}$ fibrils (Fig. S3) were recorded in tapping mode using a Veeco MultiMode instrument and Nanoscope IV controller, equipped with a fluid cell and Veeco NP-S cantilevers (0.32 N/m nominal force constant, ≈9 kHz resonant frequency in aqueous solution, 120–250 mV drive amplitude). With the AFM head removed from the instrument and inverted, the fluid cell was filled with 100 μl of dilute acetic acid (pH ≈ 3.5) and 10–20 μl of fibril solution was added. The AFM head was then lowered onto the instrument, allowing the fluid cell's O-ring to seal against a disk of freshly cleaved, dry mica. Fibrils adsorbed to the mica surface during subsequent imaging. Images were recorded at lateral scan rates of ≈10 μm/s, using the highest feedback setpoint (i.e., most gentle tapping) that was compatible with stable imaging. Images were recorded at low pH because $A\beta_{1-40}$ fibrils did not adhere to the negatively charged mica surface at neutral pH during AFM imaging.

Solid State NMR. For solid state NMR measurements, fibrils were pelleted by ultracentrifugation at 175,000 × *g* for 30 min. After discarding the supernatant, fibril pellets were resuspended in deionized water, rapidly frozen with liquid nitrogen, and lyophilized. Typical yields of lyophilized fibrils were 50–80% of the mass of initially dissolved $A\beta_{1-40}$. Material available for NMR measurements varied between 5 and 10 mg, depending mainly on

the amount of isotopically labeled Aβ_{1-40} initially available. After packing into magic-angle spinning (MAS) rotors, the lyophilized samples was rehydrated by addition of 0.5 μl of deionized water per mg of fibrils, such that a bulk water signal was observed in the ^{1}H NMR spectrum. Rehydration resulted in a significant narrowing of most NMR lines, without changing the NMR chemical shifts and without affecting cross-polarization build-up curves (Fig. S5), implying that the molecular structure was rigid and not dependent on hydration. NMR signals from labeled sites in the disordered N-terminal segment of Aβ_{1-40} had reduced intensities and slower cross-polarization build-ups after rehydration (Fig. S5). We found that water could be removed from the NMR sample by freezing and lyophilization within the MAS rotor with the rotor cap removed, and that repeated lyophilization and rehydration had reversible effects on the solid state NMR spectra.

Solid state NMR measurements were performed at 9.4 T and 14.1 T magnetic fields (399.2 MHz and 599.1 MHz ^{1}H NMR frequencies) using Varian InfinityPlus spectrometers and Varian MAS probes with 3.2 mm diameter rotors. Unless otherwise specified, ^{13}C and ^{15}N radio-frequency (rf) field strengths were 50 kHz. ^{1}H field strengths were 110 kHz for decoupling and 50 kHz plus the MAS frequency for cross-polarization. Recycle delays were 1.5 s, unless otherwise specified.

2D ^{13}C-^{13}C NMR spectra used for chemical shift assignments (Fig. 2 and Fig. S4 and Fig. S5) were obtained with finite-pulse radio-frequency-driven recoupling (fpRFDR) during the mixing period (2, 5, 6), using 15.0 μs ^{13}C π pulses, 20.0 kHz MAS, and continuous-wave decoupling in the 2.4 ms (48 rotor period) mixing period. Two-pulse phase modulated (TPPM) decoupling (7) was used during the t_1 and t_2 periods. TPPM pulse widths were typically 4.6 μs. Maximum values of t_1 and t_2 were typically 3.5–5.0 ms and 10 ms, respectively. Multidimensional data were processed using the NMRPipe software and plotted using NMRDraw (8). Linear prediction in t_1 was used to minimize artifacts in the 2D spectra arising from truncation of diagonal signals. Collection of 2D fpRFDR spectra generally required 12–24 h of signal averaging, depending on the mass of sample. Chemical shifts (referenced to tetramethylsilane) were extracted from 2D fpRFDR spectra via nonlinear regression with Gaussian functions using Mathematica.

2D ^{13}C-^{13}C NMR spectra used to detect quaternary contacts (Fig. 3 and Fig. S5) used rf-assisted diffusion (RAD (9), also known as dipolar-assisted rotational resonance (10)) in 500-1500 ms mixing periods. 2D RAD measurements were performed at MAS frequencies ranging from 15 to 20 kHz, chosen to avoid spectral perturbations due to rotational resonance effects, to enhance polarization transfers between aromatic and methyl ^{13}C atoms, and to avoid overlap of MAS sidebands with the NMR lines of interest. 2D RAD experiments required between 24 to 120 h of signal averaging, depending on the mass of the isotopically labeled sample and the intensity of the cross-peaks that contained quaternary structural information.

^{13}C-detected frequency selective rotational echo double resonance (fsREDOR) measurements (Fig. S4) were performed at 9.0 kHz MAS, as described by Jaroniec *et al.* (11) Rotor-synchronized trains of hard π pulses were applied on the ^{15}N channel, and frequency selective (1 ms) Gaussian π pulses were applied at the frequencies of the sidechain amine ^{15}N and carboxylate ^{13}C resonances in the middle of the REDOR dephasing period. S_0 and S_1 signals differed only by the presence or absence of the Gaussian ^{15}N π pulse. These measurements required ≈24 h of signal averaging for each data set.

^{15}N-detected REDOR measurements (Fig. S4) were performed with similar parameters to the ^{13}C-detected fsREDOR experiments, but with rotor-synchronized π pulses on the ^{13}C channel and with S_0 and S_1 differing by the presence or absence of the Gaussian ^{13}C π pulse. These measurements required 60 h signal averaging for the 100% isotopically labeled sample.

2D ^{15}N-^{13}C TEDOR measurements (Fig. S5) were performed at 9.0 kHz MAS as described by Jaroniec *et al.* (12) 2D TEDOR spectra were acquired in ≈24 h and 60 h of signal averaging for 2.00 ms and 3.78 ms mixing times, respectively. A 0.7 s recycle delay was used between scans.

^{13}C PITHIRDS-CT and ^{13}C-detected ^{15}N PITHIRDS-CT measurements (Fig. 3 and Fig. S4) were performed with 20.0 kHz MAS and 16.67 μs ^{13}C or ^{15}N π pulses as described previously (13). Pulsed spin-lock detection (14) was used in ^{13}C PITHIRDS-CT measurements, which required ≈12 h of signal averaging with recycle delays of 4.0 s. ^{15}N PITHIRDS-CT data sets required 48 h of signal averaging.

PITHIRDS-CT data were analyzed by comparison with numerical simulations, performed as described previously (3, 13). In simulations of ^{13}C PITHIRDS-CT data, spin polarization was placed initially on the central spin of the linear chain, and NMR signals from all spins were detected. This procedure minimizes "end effects" that would otherwise arise from the approximation of an essentially infinite system of ^{13}C nuclei by a finite system. Experimental ^{13}C PITHIRDS-CT data in Fig. 3 and Fig. S4 were corrected for contributions from natural-abundance ^{13}C signals, which were assumed to decay as a function of the dipolar evolution time at a rate that was determined from experiments on Aβ_{1-40} fibril samples with carbonyl or methyl peaks arising exclusively from natural-abundance ^{13}C.

Molecular Modeling. Molecular models were constructed in two stages of restrained simulated annealing simulations, performed using the Amber 9 suite and the ff99SB force field (available at http://amber.scripps.edu/). The first stage involved the formation of a single cross-β unit (i.e., a single molecular layer) within a fibril from six Aβ_{9-40} molecules. The first stage used all experimentally-based constraints (Table S2), except those that represent external quaternary contacts (i.e., contacts between different cross-β units). The second stage involved formation of a complete fibril segment from three preformed cross-β units, with a total of 18 Aβ_{9-40} molecules, using all experimentally-based constraints. Residues 1–8 were omitted from these simulations because experimental data show that these residues are structurally disordered.

The initial condition for the first stage was six parallel Aβ_{9-40} molecules in extended conformations, spaced 2.0 nm apart in a direction perpendicular to the peptide backbones. Simulations were performed without electrostatic interactions, starting with energy minimization to relieve strain, followed by Langevin dynamics for 100 ps. At the beginning of each Langevin dynamics simulation, the temperature was set to 100 K and atomic velocities were assigned randomly. The temperature was then increased linearly to 1000 K in 20 ps, and experimentally-based restraints were introduced with force constants increasing linearly from 0 to 10% of the values tabulated in Table S2. The simulations were allowed to proceed for an additional 40 ps at 1000 K, with restraint force constants increasing to 100% of the tabulated values over 20 ps. Finally, the temperature was reduced linearly to 100 K in 20 ps, and then linearly to 0 K in another 20 ps. Twenty independent simulations were carried out, generating 20 independent Aβ_{9-40} hexamer structures. The four lowest-energy hexamers were used as inputs for the second stage.

The second stage started with three copies of a hexamer structure from the first stage, arranged with the threefold symmetry indicated by experimental data and spaced ≈2.5 nm apart. This simulation was performed with the same protocol as in the first stage, but with additional experimentally-based restraints within the fibril core between equivalent cross-β units (I31/V39 and M35-M35 restraints in Table S2). Although the initial structure in the second stage had perfect threefold

symmetry, the final structural models have only approximate threefold symmetry because of the random velocities and random forces assigned to individual atoms in the Langevin simulations.

Each restraint applied during the simulations was a force field between two atoms, with one of two standard forms described in the Amber 9 documentation (http://amber.scripps.edu/doc9/index.html). Restraint potentials were flat over the distance or torsion angle ranges listed in Table S2, and varied outside these ranges according to parabolic functions with force constants listed in Table S2. At long range, most restraint potentials were linear. Restraints between atoms within the N-terminal β-sheet (H13, Q15, L17 and F19) and atoms within the C-terminal β-sheet (I32, L34, V36, and V40)] were represented by an alternative potential that leveled off to an asymptotic value for distances greater than $\approx$2.0 nm.

1. Petkova AT, Yau WM, Tycko R (2006) Experimental constraints on quaternary structure in Alzheimer's β-amyloid fibrils. *Biochemistry* 45:498–512.
2. Petkova AT, *et al*. (2005) Self-propagating, molecular-level polymorphism in Alzheimer's β-amyloid fibrils. *Science* 307:262–265.
3. Balbach JJ, *et al*. (2002) Supramolecular structure in full-length Alzheimer's β-amyloid fibrils: Evidence for a parallel β-sheet organization from solid-state nuclear magnetic resonance. *Biophys J* 83:1205–1216.
4. Antzutkin ON, Leapman RD, Balbach JJ, Tycko R (2002) Supramolecular structural constraints on Alzheimer's β-amyloid fibrils from electron microscopy and solid-state nuclear magnetic resonance. *Biochemistry* 41:15436–15450.
5. Ishii Y (2001) ^{13}C-^{13}C dipolar recoupling under very fast magic angle spinning in solid-state nuclear magnetic resonance: Applications to distance measurements, spectral assignments, and high-throughput secondary-structure determination. *J Chem Phys* 114:8473–8483.
6. Balbach JJ, *et al*. (2000) Amyloid fibril formation by Aβ_{16-22}, a seven-residue fragment of the Alzheimer's β-amyloid peptide, and structural characterization by solid state NMR. *Biochemistry* 39:13748–13759.
7. Bennett AE, Rienstra CM, Auger M, Lakshmi KV, Griffin RG (1995) Heteronuclear decoupling in rotating solids. *J Chem Phys* 103:6951–6958.
8. Delaglio F, *et al*. (1995) NMRpipe: A multidimensional spectral processing system based on Unix pipes. *J Biomol NMR* 6:277–293.
9. Morcombe CR, Gaponenko V, Byrd RA, Zilm KW (2004) Diluting abundant spins by isotope edited radio frequency field assisted diffusion. *J Am Chem Soc* 126:7196–7197.
10. Takegoshi K, Nakamura S, Terao T (2001) ^{13}C-^{1}H dipolar-assisted rotational resonance in magic-angle spinning NMR. *Chem Phys Lett* 344:631–637.
11. Jaroniec CP, Tounge BA, Herzfeld J, Griffin RG (2001) Frequency selective heteronuclear dipolar recoupling in rotating solids: Accurate ^{13}C-^{15}N distance measurements in uniformly ^{13}C,^{15}N-labeled peptides. *J Am Chem Soc* 123:3507–3519.
12. Jaroniec CP, Filip C, Griffin RG (2002) 3D TEDOR NMR experiments for the simultaneous measurement of multiple carbon-nitrogen distances in uniformly ^{13}C,^{15}N-labeled solids. *J Am Chem Soc* 124:10728–10742.
13. Tycko R (2007) Symmetry-based constant-time homonuclear dipolar recoupling in solid state NMR. *J Chem Phys* 126.
14. Petkova AT, Tycko R (2002) Sensitivity enhancement in structural measurements by solid state NMR through pulsed spin locking. *J Magn Reson* 155:293–299.

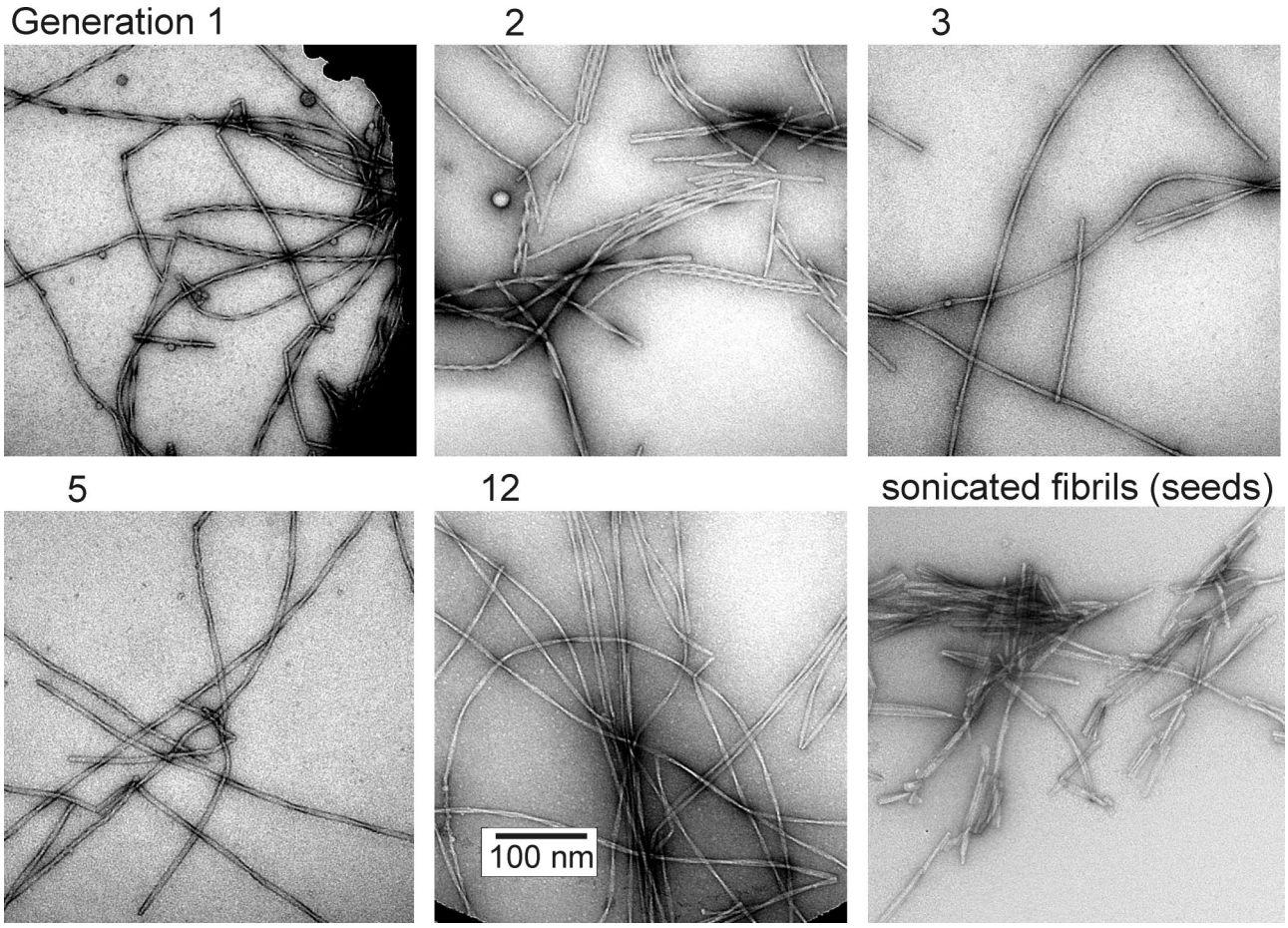

Fig. S1. Morphological purification by repeated seeding. TEM images of the initial, morphologically heterogeneous $A\beta_{1-40}$ fibril sample (generation 1) and of subsequent generations, prepared by seeded growth as described in the text and *Materials and Methods*. Multiple rounds of seeding resulted in a morphologically uniform sample by generation 12. A representative image of seeds, created by sonication of $A\beta_{1-40}$ fibrils, is shown in the lower right.

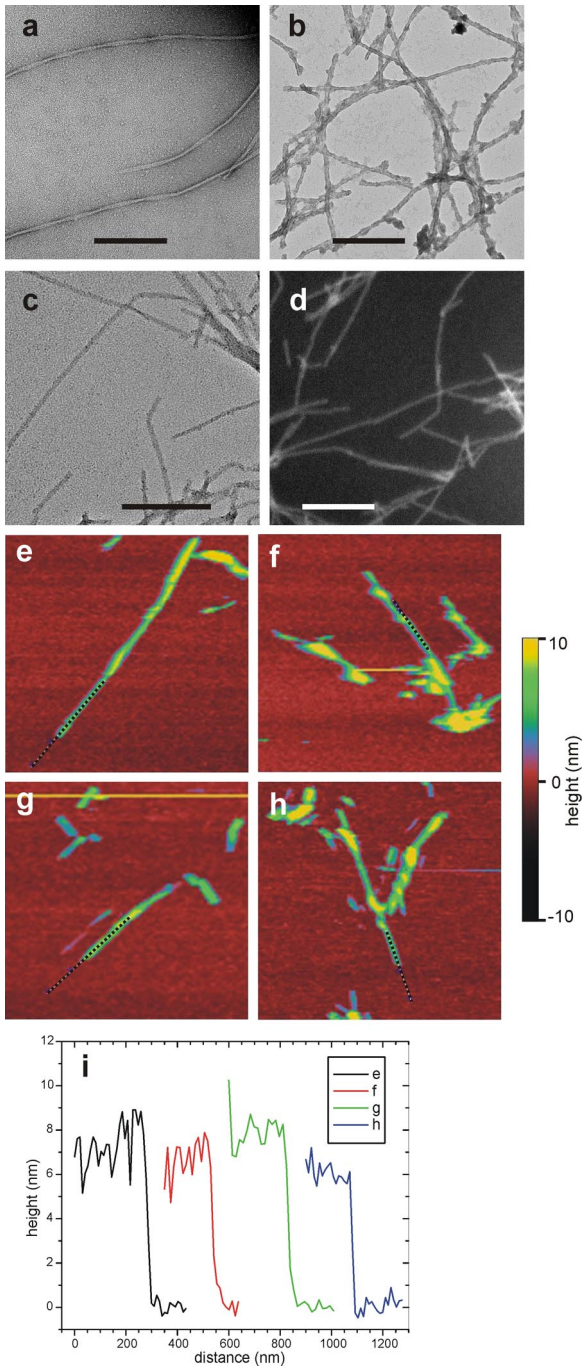

Fig. S2. Imaging of Aβ_{1-40} fibrils. (*a*) TEM image of negatively stained sample, prepared by adsorbing fibrils to carbon film from aqueous solution, rinsing with H_2O, staining with 3% uranyl acetate for 30 s, blotting, and drying in air. (*b*) TEM image of positively stained sample, prepared by 1:5 dilution of fibrils from their growth solution into 3% uranyl acetate, incubation at room temperature for 2.5 h, adsorption to carbon film, extensive rinsing with H_2O, blotting, and drying in air. (*c* and *d*) TEM images of unstained sample, prepared by adsorbing fibrils to carbon film, rinsing with H_2O, blotting, and drying in air. All images were recorded with an FEI Morgagni microscope operating at 80 kV. Images *a*–*c* are conventional bright field images; image *d* is a dark field image. Scale bars are 200 nm and paired arrows indicate 8 nm dimensions in all images. Note that a modulation of the apparent fibril width is observed only in image *a*. (*e*–*h*) Atomic force microscope images of Aβ_{1-40} fibrils with the morphology in Fig. 1*A*, recorded in solution (i.e., in the fully hydrated state). (*i*) Height profiles of fibrils along the dashed black lines in *a*–*d*. Note that fibril heights above the mica substrate are 7 $\pm$ 1 nm, consistent with the structural model in Fig. 4*B* and the picture in Fig. 1*D*.

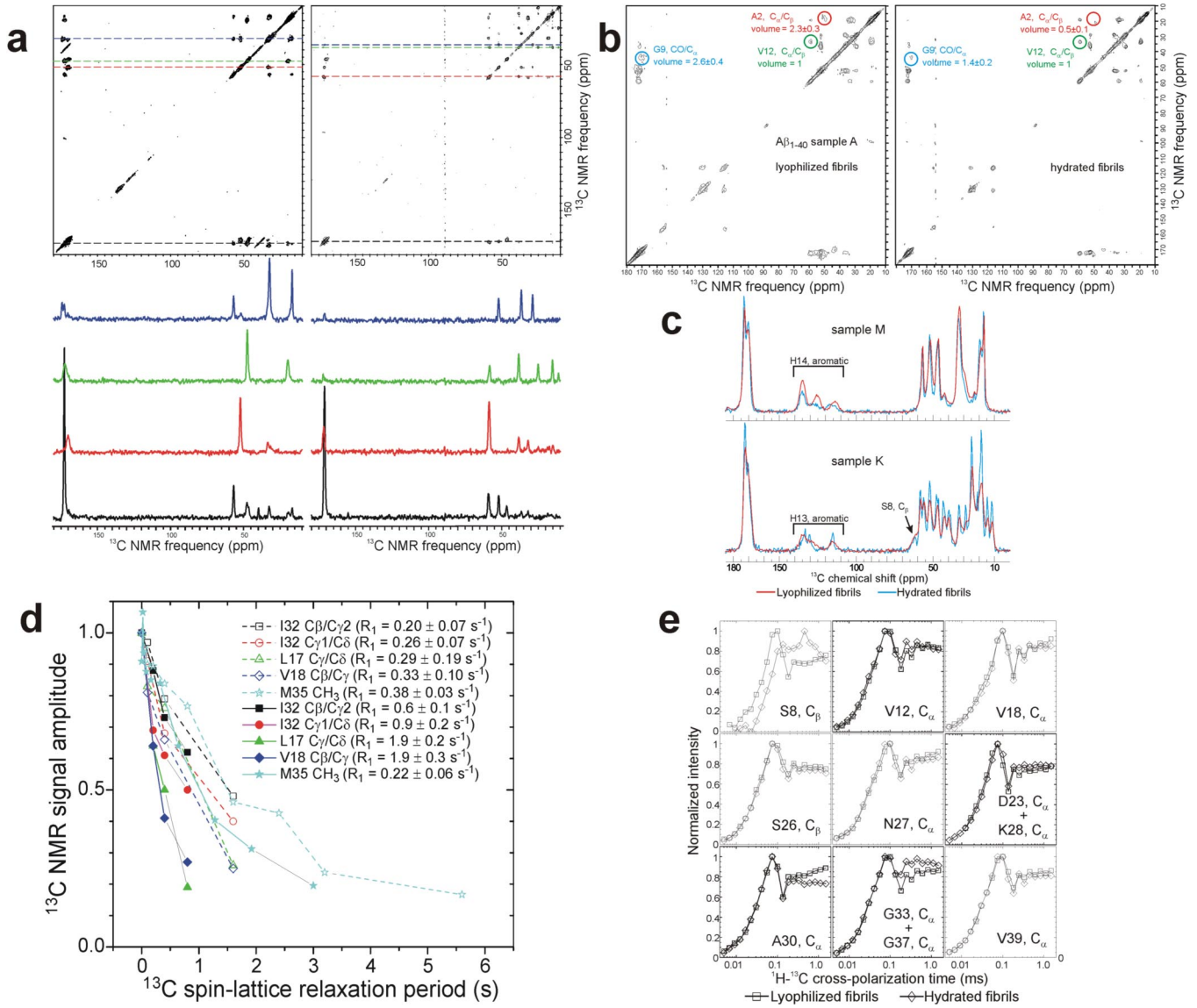

Fig. S3. ^{13}C NMR properties of Aβ_{1-40} fibrils. (*a*) Full 2D ^{13}C NMR spectra of samples M and D, respectively, with 1D slices at positions indicated by color-coded dashed lines. These slices demonstrate the signal-to-noise ratios and ^{13}C NMR linewidths that are typical of the solid state NMR data used to determine chemical shift assignments. Note that H14 sidechain cross-peaks are weak or absent, but Q15 sidechain cross-peaks (e.g., sidechain carbonyl peak at 174.1 ppm in blue slice, left side) are strong in spectra of sample M, supporting the location of the H14 sidechain on the exterior and the Q15 sidechain in the interior of the fibril structure, as in Fig. 4*b*. (*b*) Comparison of 2D ^{13}C NMR spectra of sample A in lyophilized and rehydrated states. Cross-peak volumes for A2 and G9 are reduced in the hydrated state, relative to the volume of the V12 C_α/C_β cross-peak, indicating dynamic disorder of the N-terminal segment. Strong cross-peaks among Y10 aromatic carbon sites (between 110 and 160 ppm) in the hydrated state indicate that the rigid structure begins near Y10. (*c*) 1D ^{13}C NMR spectra of samples M and K. Hydration-induced reductions in NMR intensity for the H14 aromatic and S8 C_β signals are interpreted as reductions in ^{1}H-^{13}C cross-polarization efficiency due to molecular motion. (*d*) Paramagnetic enhancement of ^{13}C spin-lattice relaxation rates in Aβ_{1-40} fibrils. Relaxation rates R_1 were measured for fibrils that were hydrated with pure H_2O (open symbols) or with 500 mM $CuNa_2$-EDTA (filled symbols). Measurements used standard double-resonance solid state NMR methods and were carried out at 9.4 T, room temperature, and 18.00 kHz MAS frequency. Signal amplitudes were measured as cross-peak volumes in a series of 2D ^{13}C NMR spectra for sample K (L17, V18, and I32 data) or peak areas in a series of 1D ^{13}C NMR spectra for sample F (M35 data). R_1 values were extracted by fitting with decaying exponential functions. The largest paramagnetic enhancements ($\Delta R_1 \approx 1.6\ s^{-1}$) were observed for L17 and V18. The smallest enhancement ($\Delta R_1 \approx 0.2\ s^{-1}$) was observed for M35. These data are consistent with burial of the M35 sidechain in the fibril core and exposure of the β-strand containing L17 and V18 to solvent. Similarity of L17 and V18 data are due to equilibration of ^{13}C spin polarizations in these sequential, uniformly ^{13}C-labeled residues through ^{13}C–^{13}C dipole–dipole couplings within the relaxation time scale. Note that the EDTA complex of Cu^{2+} would be too large to enter the fibril core. (*e*) Dependence of NMR signal intensities on ^{1}H–^{13}C cross-polarization contact time for selected ^{13}C-labeled sites. A strong effect of hydration is observed only for S8, again indicating dynamic disorder of the N-terminal segment and rigidity for residues 12–39.

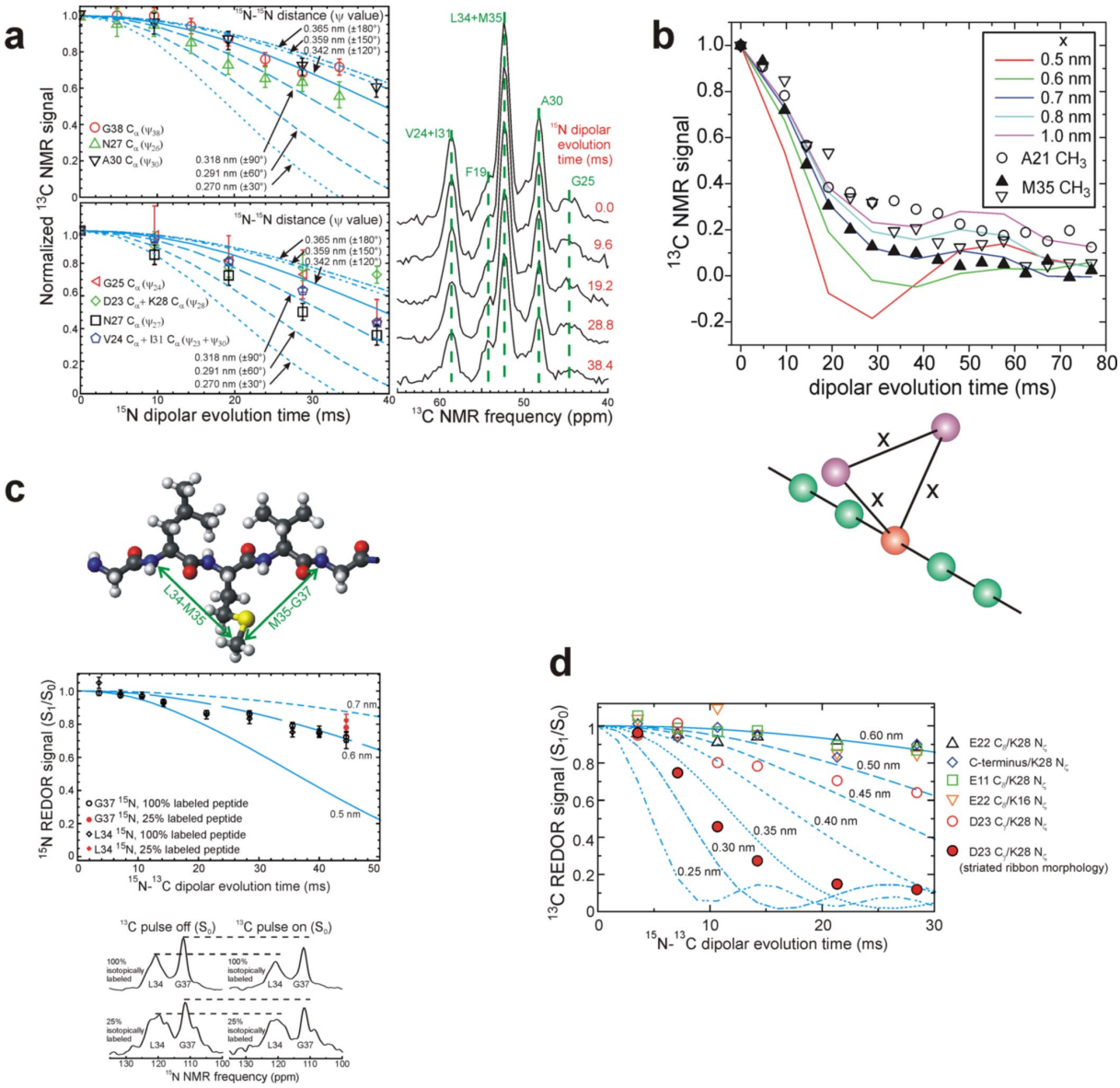

Fig. S4. Quantitative constraints on internuclear distances. (*a*) Experimental and simulated ^{15}N PITHIRDS-CT measurements of $^{15}N_i$-$^{15}N_{i+1}$ magnetic dipole-dipole couplings for sites that occur in sequential pairs of uniformly ^{15}N,^{13}C-labeled residues. In experiments, decay of ^{15}N spin polarization due to $^{15}N_i$–$^{15}N_{i+1}$ couplings is detected through $^{13}C_\alpha$ NMR signals of the indicated residues (either i or i + 1) after one-bond ^{15}N–^{13}C polarization transfer. For example, signals from G25 C_α constrain ψ of residue 24. Simulations are for sequential ^{15}N pairs with indicated distances, corresponding to the ψ angle of residue i shown in parentheses. One example of a ^{13}C-detected ^{15}N PITHIRDS-CT data set, consisting of 1D ^{13}C NMR spectra at a series ^{15}N dipolar evolution times, is shown at the *Right*. This data set yielded the A30 and G25 points. (*b*) ^{13}C PITHIRDS-CT data for the M35 C_ε and A21 C_β sites in Aβ_{1-40} fibril samples F and E, respectively. The more rapid decay and lower plateau value for the M35 data are interpreted as results of dipole–dipole couplings in the lateral direction (i.e., perpendicular to the fibril growth axis). M35 data for fibrils with the twisted morphology (filled triangles) decay more rapidly than data for fibrils with the striated ribbon morphology (open triangles). The model geometry used in simulations of the effects of lateral couplings is shown below. In addition to the five colinear spins that represent M35 C_ε sites within one cross-β unit, two spins are placed perpendicular to the five-spin chain, forming an equilateral triangle with sides *x*. Seven-spin simulations in *a* for various values of *x* show that lateral distances of ≈0.7 nm account for the experimental ^{13}C PITHIRDS-CT data for twisted fibrils. (*c*) ^{15}N-detected REDOR data for 100% isotopically labeled and 25% labeled versions of sample F. These data are measurements of ^{15}N–^{13}C dipole–dipole couplings between the M35 C_ε site and the backbone N sites of L34 and G37. Comparison with simulations (blue lines) indicates approximate 0.6 nm distances for both C_ε–N pairs, demonstrating that the M35 sidechain is not strongly tilted toward either L34 or G37 in the fibrils. The weak effect of isotopic dilution suggests that these couplings are largely intramolecular. ^{15}N NMR spectra corresponding to the data points at a dipolar evolution time of 44.4 ms in *b* for 100% and 25% labeled samples are shown below. (*d*) fsREDOR measurements of ^{15}N–^{13}C dipole–dipole couplings, with selective excitation of carboxylate carbons and amine nitrogens of the indicated residues. Comparison with simulations (blue lines) indicates a 0.5 nm ^{15}N–^{13}C distance between K28 N_ζ and D23 C_γ (open circles) in fibrils with a twisted morphology, possibly indicating a solvent-separated salt bridge interaction between K28 and D23 sidechains. Other ^{15}N-^{13}C distances in twisted fibrils are greater than 0.5 nm. In contrast, fibrils with a striated ribbon morphology (see Fig. 4*c* for comparison of morphologies) have a significantly shorter K28/D23 distance (filled circles), consistent with a direct salt bridge.

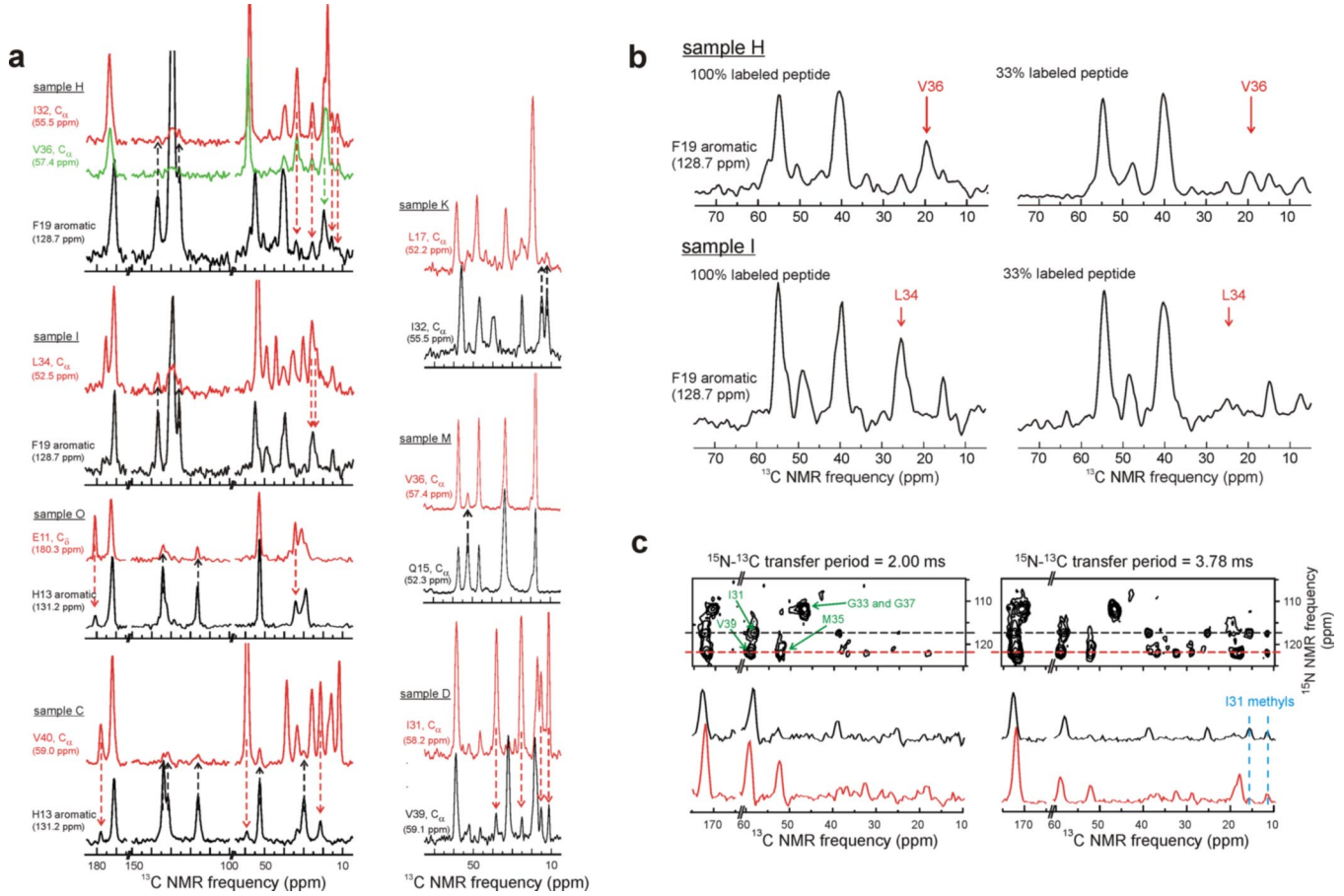

Fig. S5. Constraints on quaternary contacts. (*a*) 1D slices from 2D RAD spectra of the indicated samples. Slices are taken through the specified NMR lines of the indicated residues. Under the conditions of these measurements, all NMR lines of the indicated residues appear as strong peaks in the 1D slice, while cross-peaks to other residues appear as weaker peaks Dashed arrows point toward cross-peak signals that imply quaternary structural contacts between sidechains of pairs of labeled residues. (*b*) Comparisons of 1D slices from 2D RAD spectra for 100% labeled and 33% labeled versions of samples H and I. Isotopic dilution suppresses the F19/V36 and F19/L34 cross-peaks indicated by arrows in these slices through the F19 aromatic signal, indicating that F19/V36 and F19/L34 quaternary contacts are primarily intermolecular. The intermolecular nature of these contacts is consistent with staggering of internal quaternary contacts between β-sheets formed by N-terminal and C-terminal β-strands in $A\beta_{1-40}$ fibrils. (*c*) 2D ^{15}N-^{13}C TEDOR spectra of sample D for two values of the TEDOR polarization transfer period, with assignments of the one-bond ^{15}N-^{13}C cross-peaks. 1D slices at positions indicated by dashed lines are shown below each 2D spectrum. At the longer transfer period, multiple-bond and inter-residue cross-peaks are observed, including cross-peaks from N of V39 to sidechain methyl carbons of I31. These cross-peaks are consistent with I31/V39 quaternary contacts identified in 2D RAD spectra (part a and Fig. 3*d*).

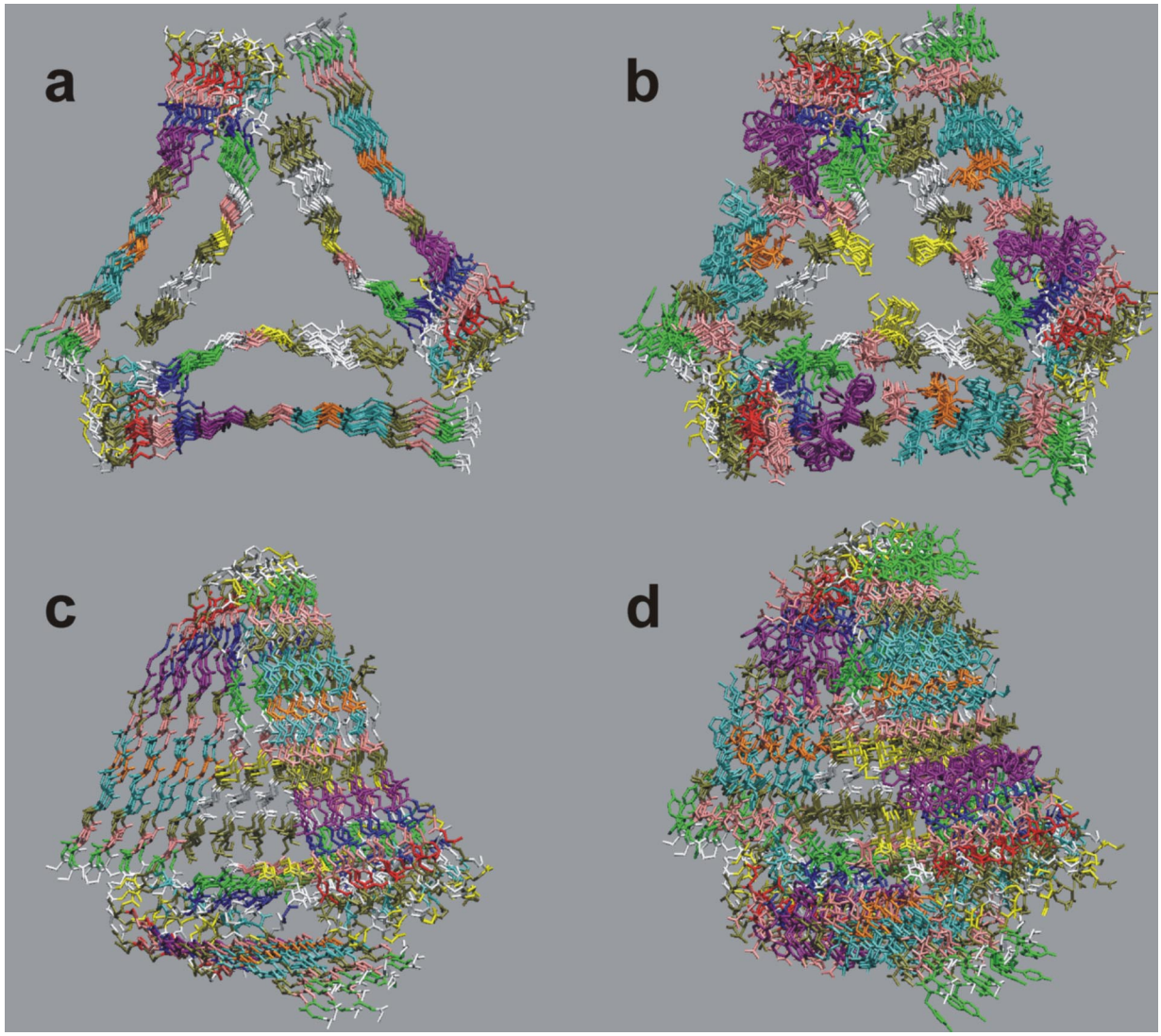

Fig. S6. Full structural models for Aβ_{1-40} fibrils with the twisted morphology. (*a* and *b*) Superposition of four low-energy structural models in a cross-sectional view, with the fibril axis perpendicular to the page. (*c* and *d*) Oblique view, rotated by ≈60° about the vertical axis. Peptide backbones only are shown in *a* and *c*. All heavy atoms are shown in *b* and *d*. Disordered residues 1–8 are omitted. For each model, the central 12 molecules from 18-molecule fibril segments are shown. These models result from simulated annealing with experimentally based restraints, as described in the main text and *Materials and Methods*. Root-mean-squared deviations from the average structure are 0.203 nm for backbone atoms and 0.228 nm for all heavy atoms.

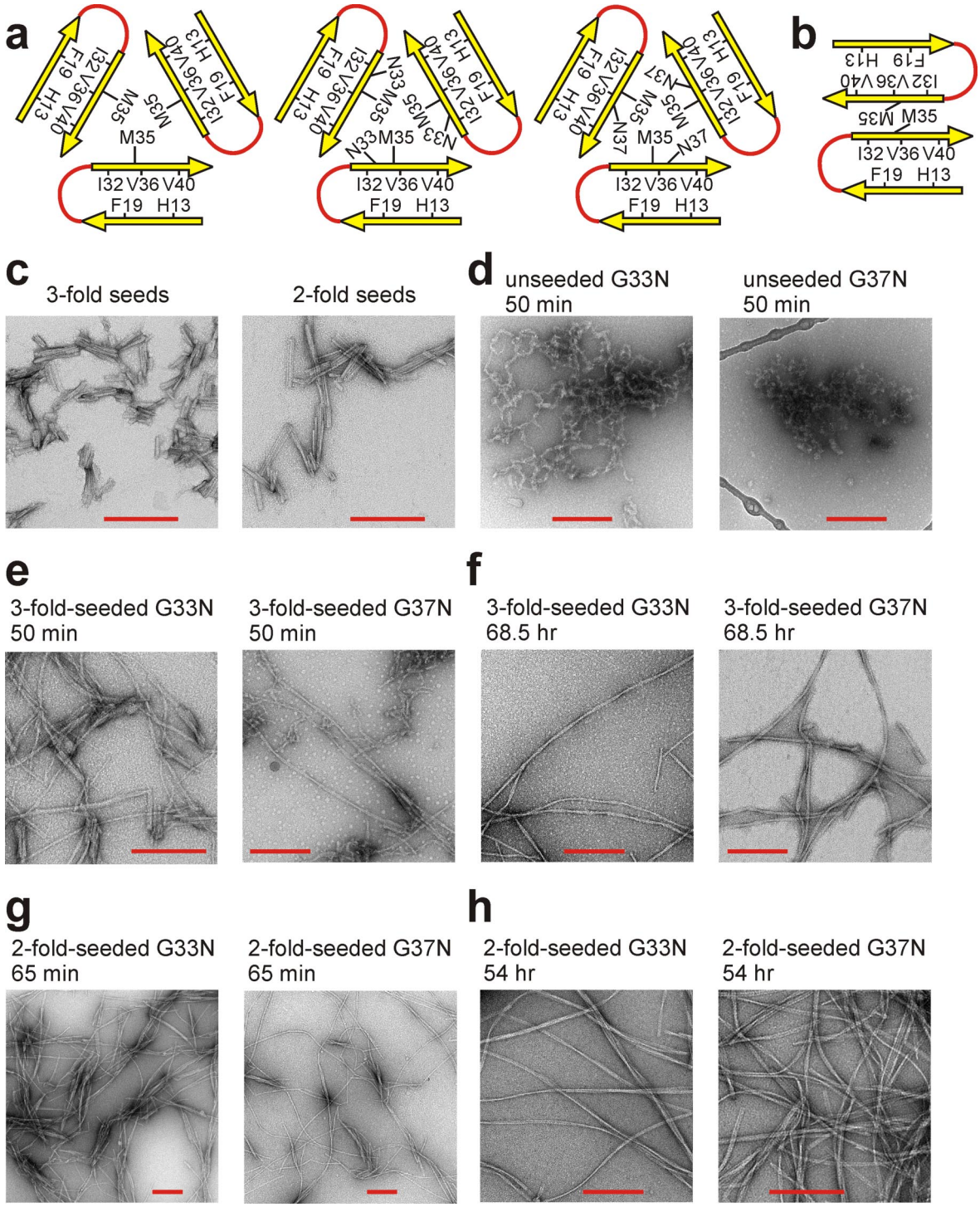

Fig. S7. Tests of structural models by mutagenesis. (*a* and *b*) Strategy for testing Aβ_{1-40} fibril models by amino acid substitutions. In *a*, the threefold symmetric model for twisted fibrils includes interior channels near M35 that can accomodate sidechains from substitutions at G33 and G37. In *b*, the twofold symmetric model for striated ribbon fibrils does not include these channels. (*c*) Wild-type fibril seeds were produced by sonication of mature twisted and striated ribbon fibrils. (*d*) Without seeding, G33N and G37N mutant peptides showed only nonfibrillar aggregates after 50 min of incubation at room temperature, 50 μM peptide concentration, 10 mM phosphate buffer, pH 7.4. No fibrils were detected by transmission electron microscopy. (*e* and *f*) With seeding by sonicated twisted fibrils (10:1 ratio of mutant to wild-type molecules in seeded solutions), fibrils were abundant after 50 min. Mature fibril morphologies replicated those of the wild-type parent fibrils, for both G33N and G37N mutants. (*g* and *h*) With seeding by sonicated striated ribbon fibrils, fibrils were also abundant after 65 min, but mature fibrils did not have the striated ribbon morphology. Thus, although wild-type striated ribbon fibrils can initiate fibril formation by G33N and G37N mutants, the striated ribbon fibril morphology (see lower image in Fig. 4*c*) is not a stable structural state for these mutants and therefore does not propagate. TEM images in *c*–*h* were recorded with negative staining, using an FEI Morgagni microscope operating at 80 kV. [Scale bars: 200 nm in all images.]

Table S1. ^{13}C NMR chemical shifts in Aβ_{1-40} fibrils

	^{13}C NMR chemical shift, ppm							
Residue	CO	C_α	C_β	$C\gamma$	C_δ	C_ε	C_ξ	TALOS ϕ,ψ predictions, °
A2	173 ± 1 (176.1)	49 ± 2 (50.8)	21 ± 2 (17.4)					—
G9	170.5 ± 1 (173.2)	44.5 ± 1 (43.4)						—
Y10	172 ± 1 (174.2)	52.5 ± 1 (56.2)	36 ± 1 (37.1)	129.8 (128.9)	131.2 (131.6)	116.3 (116.5)	155.4 (155.6)	—
E11	171.5 (174.9)	52.8 (54.9)	29.7 (28.2)	34.4 (33.9)	180.3 (181.7)			−128 ± 18, 141 ± 21
V12	172.4 (174.6)	59.3 (60.5)	33.7 (31.2)	19.2 ± 1.0 (19.4,18.6)				−124 ± 7, 132 ± 13
H13	171.2 (172.4)	52.5 (53.3)	29.5 (27.3)	131.2 (129.4)	116.2 (118.4)	135.6 (134.5)		−113 ± 14, 127 ± 6
H14	170.2 (172.4)	52.0 (53.3)	33.7 (27.3)	128.4 ± 1.0 (129.4)	114.5 ± 1.0 (118.4)	135.5 (134.5)		−127 ± 23, 149 ± 11
Q15	170.2 (174.3)	52.3 (54.0)	32.8 (27.7)	33.7 (32.0)	174.1 (178.8)			−128 ± 12.5, 145 ± 16
K16	171.8 (174.9)	52.6 (54.5)	34.3 (31.4)	23.9 (23.0)	28.2 (27.3)	40.2 (40.2)		−126 ± 16, 136 ± 9
L17	173.0 (175.9)	52.2 (53.4)	43.2 (40.7)	26.9 (25.2)	25.7, 21.9 (23.2, 21.6)			−110 ± 19, 1301 ± 13
V18	172.4 (174.6)	58.9 (60.5)	33.6 (31.2)	19.3,18.9 (19.4,18.6)				−1281 ± 7, 129 ± 12
F19	171.0 (174.1)	54.4 (56.0)	40.5 (37.9)	136.5 (137.2)	129.0 (130.2)	128.0 (129.8)	125.3 (128.2)	−124 ± 11, 129 ± 13
F20	170.6 (174.1)	54.3 (56.0)	41.2 (37.9)	137.5 (137.2)	129.3 (130.2)	128.8 (129.8)	126.9 (128.2)	−126 ± 16, 140 ± 19
A21	173.4 (176.1)	48.0 (50.8)	20.4 (17.4)					−131 ± 21, 146 ± 15
E22	174.3 (174.9)	52.7 (54.9)	32.2 (28.2)	34.3 (33.9)	181.3 (181.7)			−128 ± 9, 145 ± 18
D23*	172.5	53.0	36.3	179.0				—
	174.3 (174.6)	53.5 (52.5)	38.8 (39.4)	177.5 (178.3)				
V24	174.4 (174.6)	58.3 (60.5)	32.4 (31.2)	18.8 (19.4,18.6)				—
G25	171.6 (173.2)	44.0 (43.4)						—
S26†	171.9 (172.9)	53.8 (56.6)	63.7 (62.1)					−116 ± 23, 145 ± 21
N27†	172.4 (173.5)	51.6 (51.4)	39.0 (37.2)	174.2 (175.5)				−112 ± 19, 133 ± 23
K28†	173.8 (174.9)	52.4 (54.5)	33.6 (31.4)	23.1 (23.0)	28.1 (27.3)	40.1 (40.2)		−133 ± 12, 135 ± 17
G29	169.9 (173.2)	43.0 (43.4)						—
A30†	172.8 (176.1)	48.4 (50.8)	19.5 (17.4)					−125 ± 20, 153 ± 18
I31	171.9 (174.7)	58.2 (59.4)	38.5 (37.1)	25.2,15.3 (25.5,15.7)	11.3 (11.2)			−115 ± 11, 123 ± 12
I32	174.0 (174.7)	55.5 (59.4)	40.7 (37.1)	25.3, 15.5 (25.5,15.7)	12.4 (11.2)			−127 ± 12, 142 ± 14
G33	170.0 (173.2)	46.4 (43.4)						—
L34	171.5 (175.9)	52.5 (53.4)	44.1 (40.7)	25.5 (25.2)	23.4, 21.1 (23.2, 21.6)			−129 ± 8, 153 ± 15
M35	171.2 (174.6)	52.4 (53.7)	34.7 (31.2)	30.0 (30.3)		15.6 (15.2)		−127 ± 20, 140 ± 14
V36	172.6 (174.6)	57.4 (60.5)	32.9 (31.2)	18.9,17.4 (19.4,18.6)				−137 ± 18, 150 ± 25
G37	168.9 (173.2)	45.8 (43.4)						—
G38	169.1 (173.2)	43.0 (43.4)						—
V39	171.6 (174.6)	59.1 (53.7)	32.2 (31.2)	18.8 (19.4,18.6)				−118 ± 15, 132 ± 13
V40	177.9	59.0 (53.7)	33.2 (31.2)	21.2 (19.4,18.6)				—

Shifts are relative to tetramethylsilane, with uncertainties of approximately ±0.2 ppm except where indicated. Note that these chemical shifts apply specifically to fibrils with the morphological characteristics in Figure 1 of the main text. Values in parentheses are random coil shifts [Wishart DS, Bigam CG, Holm A, Hodges RS, Sykes BD (1995) 1H, 13C and 15N random coil NMR chemical shifts of the common amino acids. I. Investigations of nearest-neighbor effects. *J Biomol NMR* 5:67–81], adjusted to the tetramethylsilane reference. Predicted ϕ,ψ torsion angles from the TALOS program [Cornilescu G, Delaglio F, Bax A (1999) Protein backbone angle restraints from searching a database for chemical shift and sequence homology. *J Biomol NMR* 13:289–302] are given when at least 9 of the 10 best matches from the TALOS database were in the same secondary structure region. Torsion angle values and uncertainties represent the averages and standard deviations of the TALOS matches.

*D23 exhibits two sets of ^{13}C chemical shifts, attributed to intrinsic disorder of the D23 sidechain.

†bTALOS predictions for these residues were not used as restraints in Langevin dynamics simulations to generate Aβ_{9-40} fibril models. Backbone conformations of these residues were restrained instead by backbone N_i-N_{i+1} distance measurements.

Table S2. Summary of restraints employed in modeling of Aβ_{1-40} fibril structure

Restraint		Force constant	Value	Experimental basis
Backbone torsion angles ϕ and ψ		100 kcal/mol-rad^2	see Table S1	TALOS predictions from ^{13}C NMR chemical shifts (Table S1)
Nearest-neighbor intermolecular distances between backbone N and O of β-strand residues 2j and backbone O and N of residues 2j $-$ 1 and 2j $+$ 1, respectively		2,000 kcal/mol-nm^2	0.275–0.315 nm	In-register parallel β-sheets indicated by ^{13}C PITHIRDS-CT data (Fig. 3 *A* and *B*)
Nearest-neighbor intermolecular distances among M35 or A21 sidechain methyl carbons within a single cross-β unit		2,000 kcal/mol-nm^2	0.45–0.55 nm	^{13}C PITHIRDS-CT data (Fig. 3 *A* and *B*)
Distances between sidechain carbons in the following residue pairs*†: H13/V40; Q15/V36; L17/I32; F19/I32; F19/L34; F19/V36		1,000 kcal/mol-nm^2	$<$0.6 nm	Inter-residue cross-peaks in 2D RAD spectra (Fig. 3 *C* and *E* and Fig. 9)
Distance between D23 C_γ and K28 sidechain N		1,000 kcal/mol-nm^2	0.45–0.55 nm	fsREDOR data (Fig. 13)
Intramolecular backbone N_i–N_{i+1} distances	D23-V24	10,000 kcal/mol-nm^2	0.291–0.334 nm	^{15}N PITHIRDS-CT data (Fig. 8)
	V24-G25		0.326–0.400 nm	
	S26-N27		0.318–0.342 nm	
	N27-K28		0.300–0.326 nm	
	K28-G29		0.342–0.400 nm	
	A30-I31		0.342–0.353 nm	
Intramolecular distances from M35 methyl to L34 and G37 N		1,000 kcal/mol-nm^2	0.5–0.7 nm	^{15}N-detected REDOR (Fig. 12)
Distances between sidechains of I31 and V39 from different cross-β units[b]		1,000 kcal/mol-nm^2	$<$ 0.6 nm	Inter-residue crosspeaks in 2D RAD spectra (Fig. 3*D* and Fig. 9) TEDOR data (Fig. 13)
intermolecular distances among M35 methyl carbons from different cross-β units		1000 kcal/mol-nm^2	0.65–0.75 nm	^{13}C PITHIRDS-CT data (Fig. 11)

*These distances are modeled as intermolecular distances with staggering by two peptide chains [see Petkova AT, Yau WM, Tycko R (2006) Experimental constraints on quaternary structure in Alzheimer's beta-amyloid fibrils. *Biochemistry* 45:498–512], consistent with isotopic dilution experiments in Fig. S2.
†These distance restraints were applied between the terminal carbons of the relevant sidechains.